Optical Beam Jitter Control for the NPS HEL Beam Control Testbed

Jae Jun Kim, Masaki Nagashima, and Brij. N. Agrawal
Naval Postgraduate School, Monterey, CA, 93943

In this paper, an optical beam jitter control method for the Naval Postgraduate School HEL beam control testbed is presented. Additional hardware is developed and integrated on the testbed to realize the strap-down IRU jitter compensation architectures. Feedforward control design of the strap-down IRU design is studied and tested on the testbed. An adaptive filtering method for narrow-field-of-view video tracker jitter correction is also presented.

I. INTRODUCTION

For directed energy systems, maintaining a stable line-of-sight with passive and active compensation of optical beam jitter is a critical element. Typical disturbance sources contributing to optical jitter include platform vibration, structural flexibility, dynamic loading, acoustics, atmospheric jitter and beam path conditioning effects. The control system should be designed to minimize optical jitter under these various disturbance sources. A well-designed optical jitter control system not only increases the effectiveness of the directed energy system, but it also enhances the imaging and tracking capabilities that will share the same optical path.

The Naval Postgraduate School (NPS) developed a laboratory HEL beam control testbed to study beam control technologies related to acquisition, pointing, tracking, adaptive optics, and optical beam jitter control. The testbed is designed to provide an end-to-end beam control demonstration of HEL systems.

An optical Inertial Reference Unit (IRU) is a key element for optical jitter control to provide an inertially stabilized reference laser. Since most of the optical jitter is due to its own system platform variations, an IRU is integrated into the system such that its reference beam samples most disturbances in the optical path. The original design of the NPS HEL beam control testbed does not include the IRU and the use of the reference laser available on the testbed was limited to the optical path alignment functions. Therefore, jitter control capabilities are significantly limited in the NPS testbed, especially for higher frequency disturbances that cannot be addressed with the video tracking system.

An IRU system typically employs a complex stabilized platform system to produce an inertially stable laser. Since development and implementation of a platform-based IRU system is a complex and expensive task, we explored alternative strap-down IRU schemes.

With strap-down IRU schemes, the correction is open-loop and requires an accurate calibration of the gain and phase of the feedforward path (Perram et al. 2010). However, accurate system identification and modeling of an IRU system may not guarantee consistent jitter control performance and repeated calibration may be necessary.

NPS has focused on developing adaptive filters for use in the control of optical beam jitter in spacecraft applications and optical beam control systems. The basic principle of an adaptive filter working in an adaptive algorithm is that controller gains can be varied throughout the control process to adapt to changing parameters and can therefore cancel disturbances more effectively than passive methods. Various adaptive control algorithms have been developed for active noise control (Widrow & Stearns 2002; Elliott & Nelson 1985; Haykin 2002; Kuo 1996). At NPS, various adaptive control algorithms have been investigated (Edwards 1999; Watkins 2007; Yoon 2008; Beerer 2008) to attenuate jitter due to narrowband and broadband disturbances.

In this paper, various ways to improve optical jitter control capabilities of the testbed are investigated. Additional hardware is developed and integrated on the testbed to realize the strap-down IRU jitter compensation architectures. Feedforward control design of the strap-down IRU design is studied and tested on the testbed. An adaptive filtering method for narrow-field-of-view video tracker jitter correction is also presented.

Report Documentation Page

Form Approved
OMB No. 0704-0188

1. REPORT DATE	2. REPORT TYPE	3. DATES COVERED
NOV 2011		**00-00-2011 to 00-00-2011**

4. TITLE AND SUBTITLE	5a. CONTRACT NUMBER
Optical Beam Jitter Control for the NPS HEL Beam Control Testbed	5b. GRANT NUMBER
	5c. PROGRAM ELEMENT NUMBER
6. AUTHOR(S)	5d. PROJECT NUMBER
	5e. TASK NUMBER
	5f. WORK UNIT NUMBER
7. PERFORMING ORGANIZATION NAME(S) AND ADDRESS(ES) **Naval Postgraduate School,Spacecraft Research & Design Center,699 Dyer Road,Monterey,CA,93943-5106**	8. PERFORMING ORGANIZATION REPORT NUMBER
9. SPONSORING/MONITORING AGENCY NAME(S) AND ADDRESS(ES)	10. SPONSOR/MONITOR'S ACRONYM(S)
	11. SPONSOR/MONITOR'S REPORT NUMBER(S)

12. DISTRIBUTION/AVAILABILITY STATEMENT
Approved for public release; distribution unlimited

13. SUPPLEMENTARY NOTES
14th Annual Directed Energy Symposium, 14-18 November 2011, San Diego 11-Symp-080

14. ABSTRACT

15. SUBJECT TERMS

16. SECURITY CLASSIFICATION OF:			17. LIMITATION OF ABSTRACT	18. NUMBER OF PAGES	19a. NAME OF RESPONSIBLE PERSON
a. REPORT **unclassified**	b. ABSTRACT **unclassified**	c. THIS PAGE **unclassified**	**Same as Report (SAR)**	**10**	

II. NPS HEL BEAM CONTROL TESTBED

The objective of the testbed is to provide a research environment for the development of new technologies related to acquisition, pointing, tracking, adaptive optics and jitter control and to provide an end-to-end beam control demonstration of HEL systems. A picture of the testbed is shown in Figure 1.

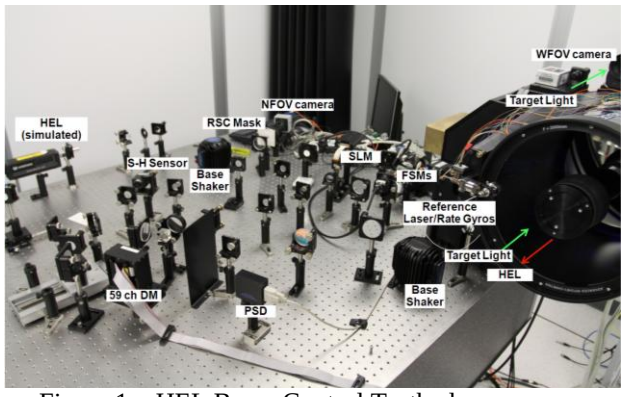

Figure 1. HEL Beam Control Testbed

The testbed has a rate gyro stabilized gimbaled telescope with a 10-inch primary mirror, Wide Field of View (WFOV) and Narrow Field of View (NFOV) Camera Systems, Fast Steering Mirrors (FSMs), a Position Sensing Detector (PSD) sensor for jitter control and fine beam steering, a Deformable Mirror (DM), a Shack-Hartmann wavefront sensor for Adaptive Optics (AO), a Spatial Light Modulator (SLM) for atmospheric disturbance simulation, and base shakers for disturbance generation.

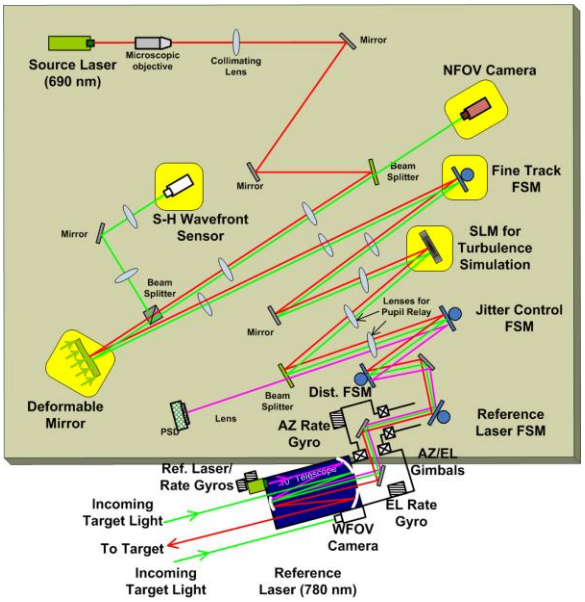

Figure 2. Schematic of the beam control testbed

Current schematic of the testbed is shown in Figure 2. The testbed setup is constantly modified and tested to upgrade its capabilities and study trade-offs between various system design architecture.

Figure 3 depicts the operation of the testbed when the laser is engaged to the target. The diagnostic target station employs target lights and a PSD to test various scenarios and measure the performance.

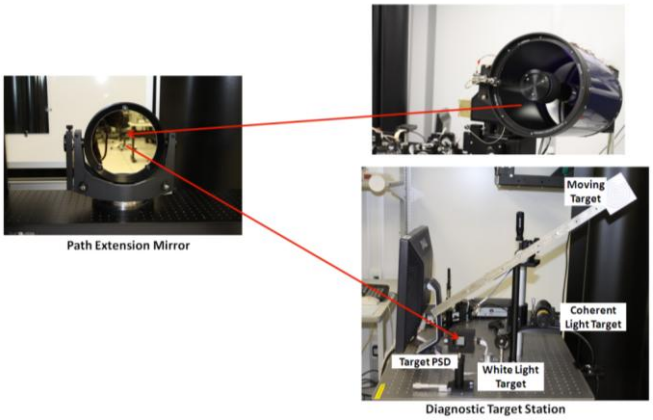

Figure 3. Testbed operation

III. STRAP-DOWN INERTIAL REFERENCE UNIT

Initial setup of the reference laser is not inertially stabilized. The reference laser source component moves with the telescope tube and the movement of the telescope along the gimbal axes or the movement of the entire platform cannot be detected by observing the reference beam. Therefore, correction of the optical jitter is limited to the jitter observed in the reference beam path, and any other jitter that cannot be observed will remain in the system.

An inertially stabilized reference beam can detect jitters throughout the entire optical path of the system, and an Inertial Reference Unit (IRU) system employing a stabilized platform to produce a jitter-free reference beam is one of the solutions to obtain an inertially stabilized reference beam. But development and implementation of such a unit is a complex and expensive task, so other solutions were explored for the testbed.

A full scale IRU can be downsized and simplified by replacing the stabilized platform with a fast-steering mirror and inertial sensors attached to the location of the reference laser source to measure the local vibration. Figure 4 shows two approaches considered in the project for implementation of a "strap-down" IRU system.

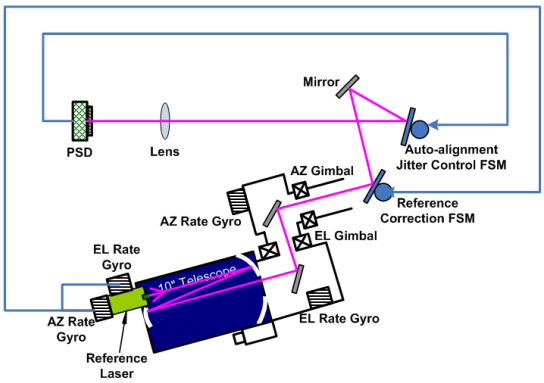

(a) Method 1

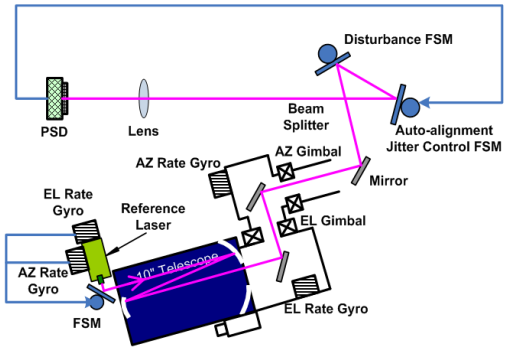

(b) Method 2

Figure 4. Strap-down IRU Implementation by Two Different Methods

For method 1, two rate gyros are attached to the location of the reference laser unit and the output signal from the gyros are sent to the fast-steering mirror located on the optical bench. A feedforward control algorithm implemented for the fast-steering mirror will compensate the jitter that cannot be observed by the reference laser beam using the information from the gyro sensors.

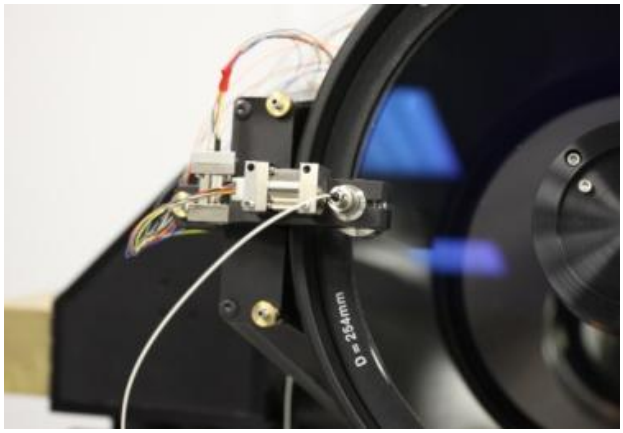

Figure 5. Implementation of Method 1 Using ARS-15 Rate Sensors

Method 2 also employs two rate gyros, but the compensation for the vibration of the laser source unit is made at the laser source, such that the resulting reference beam is inertially stabilized. The hardware components developed for the integration of these methods are shown in Figure 5 and Figure 6. Several gyro sensors were tested for sufficient performance, and the ARS-15 MHD angular rate sensor by Applied Technology Associates was chosen for its size and performance.

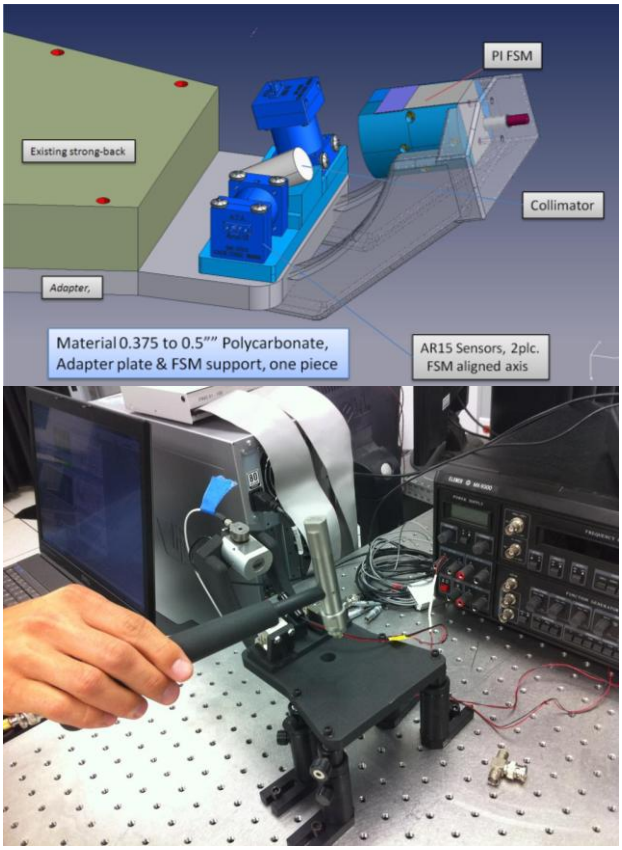

Figure 6. Strap-Down IRU Design and Hardware Testing for Method 2

IV. FEEDFORWARD CONTROL FOR STRAP-DOWN IRU

In the strap-down IRU represented in Figure 4, a pair of gyro sensors are used to detect the angular motion of the reference laser and a feedforward control is applied which generates the command for FSMs that eliminate jitter in the reference beam. The feedforward control method presented in this section is based on Method 1 shown in Figure 4(a).

To succeed in feedforward control by the rate gyro signals, the transfer function from the gyro output to the jitter caused by the movement of the reference laser must be known. This transfer function was developed by using a two-step process. The first step was to determine the

transfer function between the jitter measured by the onboard PSD. This was done by shooting the laser beam from the target and observing it by the PSD on the testbed while an excitation signal was applied to the gimbals. The second step was to obtain the transfer function from the command to the FSM to be used for feedforward control to the movement of the beam from the same PSD on the testbed. The feedforward control problem can be formulated as follows:

Assume the following linear relationship:

$$X_{PSD}(z) = T_{AZ}(z) X_{Gyro}(z) \quad (1)$$

$$Y_{PSD}(z) = T_{EL}(z) Y_{Gyro}(z) \quad (2)$$

where $X_{PSD}(z)$ and $Y_{PSD}(z)$ are the horizontal and vertical axes output of the PSD measuring the position of the stationary laser beam from the target, and $X_{Gyro}(z)$ and $Y_{Gyro}(z)$ are azimuth and elevation axes rate measurements by the gyros attached at the end of the telescope tube. The objective of the feedforward control is to cancel the disturbance by a FSM whose dynamics are given as follows:

$$X'_{PSD}(z) = G_{AZ}(z) X_{FSM}(z) \quad (3)$$

$$Y'_{PSD}(z) = G_{EL}(z) Y_{FSM}(z) \quad (4)$$

The command to the FSM, $X_{FSM}(z)$ and $Y_{FSM}(z)$, needs to satisfy:

$$X_{PSD}(z) - X'_{PSD}(z) = T_{AZ}(z) X_{Gyro}(z) - G_{AZ}(z) X_{FSM}(z) = 0 \quad (5)$$

$$Y_{PSD}(z) - Y'_{PSD}(z) = T_{EL}(z) Y_{Gyro}(z) - G_{EL}(z) Y_{FSM}(z) = 0 \text{ , } (6)$$

which leads to:

$$X_{FSM}(z) = -G_{AZ}(z)^{-1} T_{AZ}(z) X_{Gyro}(z) \quad (7)$$

$$Y_{FSM}(z) = -G_{EL}(z)^{-1} T_{EL}(z) Y_{Gyro}(z) \text{ .} \quad (8)$$

1. Gyro-PSD Path Measurement

The frequency response of the transfer function relating the gyro signal to that of the PSD can be obtained by measuring the frequency responses of the PSD and gyro output to the excitation applied to the gimbal and taking the ratio as follows:

$$T_{AZ}(e^{j\omega T}) = \frac{X_{PSD}(e^{j\omega T})}{X_{Gyro}(e^{j\omega T})} \quad (9)$$

$$T_{EL}(e^{j\omega T}) = \frac{Y_{PSD}(e^{j\omega T})}{Y_{Gyro}(e^{j\omega T})} \quad (10)$$

Experiments were conducted to measure the frequency response of the sensors. A target laser was set up about 12 m away from the telescope. $X_{PSD}(e^{j\omega T})$ and $X_{Gyro}(e^{j\omega T})$ were measured while applying an excitation sinusoid of frequency ω (rad) to the azimuth gimbal, and $Y_{PSD}(e^{j\omega T})$ and $X_{Gyro}(e^{j\omega T})$ were measured while the same disturbance was applied to the elevation gimbal. Range of the excitation frequencies used in the experiment is from 2 Hz to 15 Hz with 0.5 Hz intervals. For more accuracy, the frequency response measurement was obtained for each excitation frequency separately by applying a single sinusoid at a time, instead of the sine sweep method where the frequency is continuously changing. The obtained frequency responses are shown in Figure 7 and Figure 8.

Since the PSD measurement is proportional to the angle of the telescope and the gyro measurement is the derivative of this angle, the transfer function representing the PSD to the gyro path is expected to involve a differentiator. In addition, the flexible nature of the telescope structure is likely to have non-minimum phase dynamics which result in unstable zeros. The transfer function of the gyro to the PSD path is the inverse of this transfer function and therefore unstable due to the integrator and unstable poles. This poses a problem because the transfer functions $T_{AZ}(z)$ and $T_{EL}(z)$ are used to compute the FSM command and they have to be stable and causal.

It is, however, possible to obtain a stable transfer function that approximates the unstable transfer function for a limited frequency range. From the experimental data, approximated transfer functions $\hat{T}_{AZ}(z)$ and $\hat{T}_{EL}(z)$ were obtained as follows:

$$\hat{T}_{AZ}(z) = 18.4592 \cdot T_{IIR}(z) T_{ave}(z) \quad (11)$$

$$\hat{T}_{EL}(z) = 20.7145 \cdot T_{IIR}(z) T_{ave}(z) \quad (12)$$

$$T_{ave}(z) = \frac{1}{N} \sum_{n=0}^{N} z^{-n} \quad (13)$$

$$T_{IIR}(z) = \frac{(z - 0.7515)\ (z - 0.8234)\ (z - 1)\ (z - 0.04321)}{z\ (z - 0.9978)\ (z - 0.9977)\ (z - 0.99)} \quad (14)$$

Since the shapes of the frequency response in Figure 7 and Figure 8 are almost identical, the transfer functions were approximated by a transfer function Eq. (100) with different coefficients. A FIR filter of N average, which does not significantly affect the gain and phase in the frequencies of interest, was also applied to remove the low frequency components where the signal to noise ratio of the gyro is too low. Figure 7 and Figure 8 show

that the obtained models agree with the measurements in the frequency range between 6 Hz and 10 Hz.

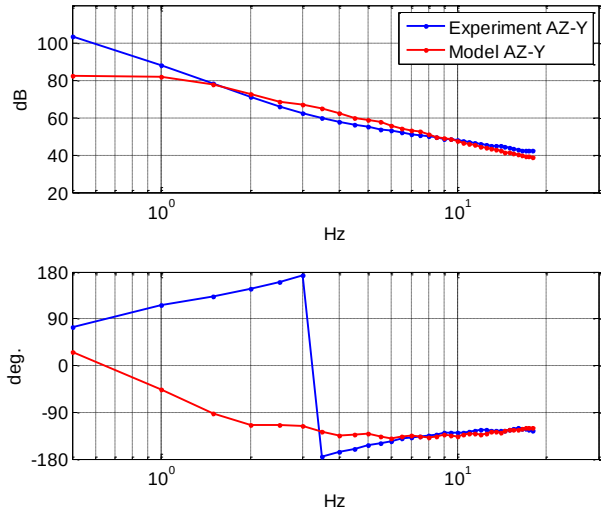

Figure 7. Model of azimuth axis frequency response from gyro to PSD

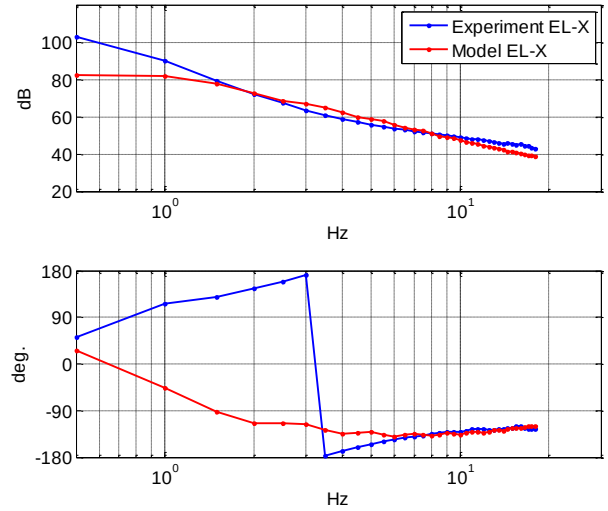

Figure 8. Model of elevation axis frequency response from gyro to PSD

2 FSM-PSD Path Measurement

Figure 9 and Figure 10 show the frequency response of the FSM - PSD paths related to X and Y axes, respectively. They indicate that the transfer function can be well approximated by a scalar constant, ignoring the dynamics for the frequencies below 10 Hz, which is the frequency range of interest for this experiment.

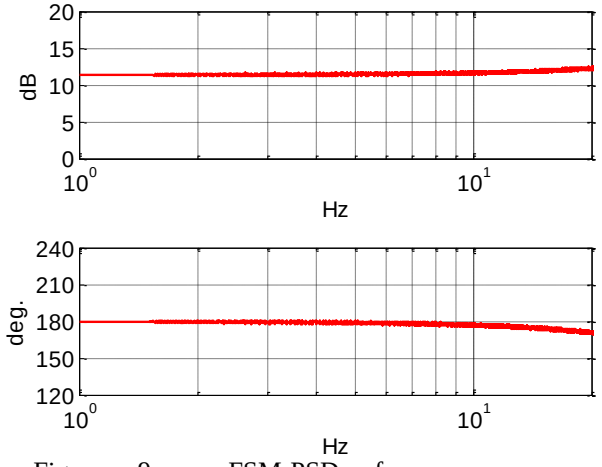

Figure 9. FSM-PSD frequency response corresponding to azimuth axis

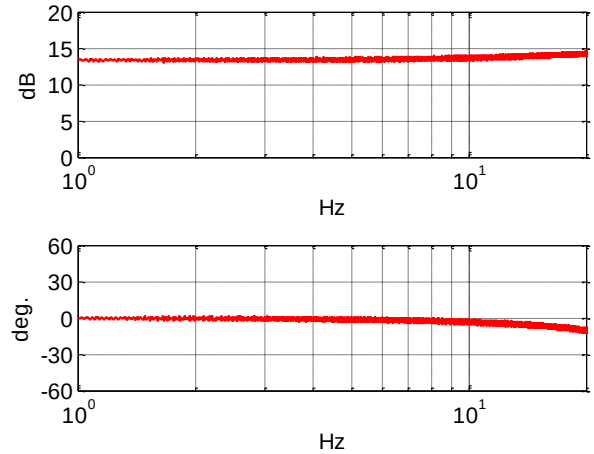

Figure 10. FSM-PSD frequency response corresponding to elevation axis

Now the inverse of the FSM - PSD dynamics also becomes a constant and the formulae for FSM commands are reduced to the following:

$$Y_{FSM}(z) = g_{EL} T_{EL}(z) Y_{Gyro}(z) \quad (15)$$

$$X_{FSM}(z) = g_{AZ} T_{AZ}(z) X_{Gyro}(z) \quad (16)$$

The magnitudes of g_{AZ} and g_{EL} are proportional to the distance from the FSM to the PSD and the signs depend on the configuration of the optical system. Through some experiments, the following constants were obtained and used for the controller:

$$g_{AZ} = 0.2683 \quad (17)$$

$$g_{EL} = -0.2137 \quad (18)$$

3 *Experimental Results*

Figure 11 and Figure 12 show the error measured by the PSD at the target when a 7 Hz disturbance was applied to the azimuth gimbal. Figure 13 and Figure 14 show when the disturbance was applied to the elevation gimbal.

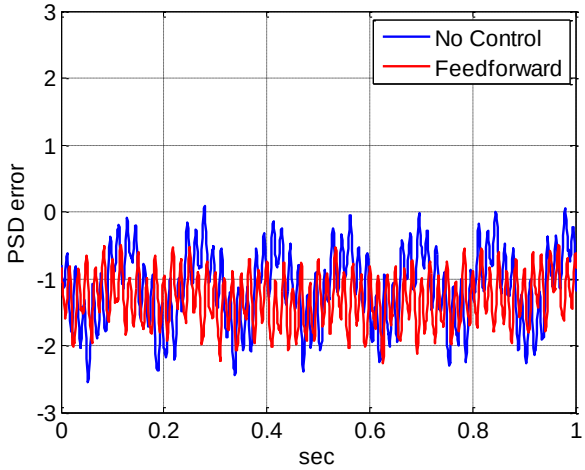

Figure 11. Time domain PSD X-axis error for azimuth disturbnace

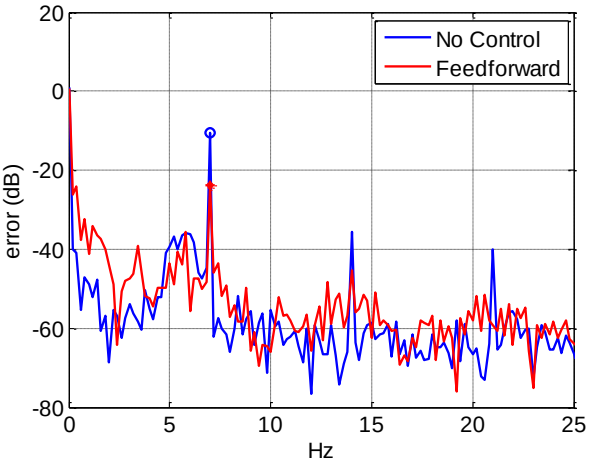

Figure 12. Spectrum of the PSD X-axis error for azimuth disturbance

The magnitude of the command to the gimbal is the same for each axis, but since the azimuth gimbal is heavier from carrying the elevation gimbal, it produces less disturbance than the elevation gimbal.

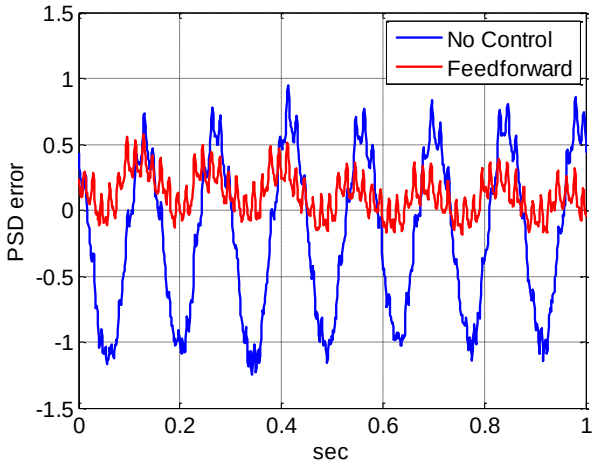

Figure 13. Time domain PSD Y-asis error for elevation disturbance

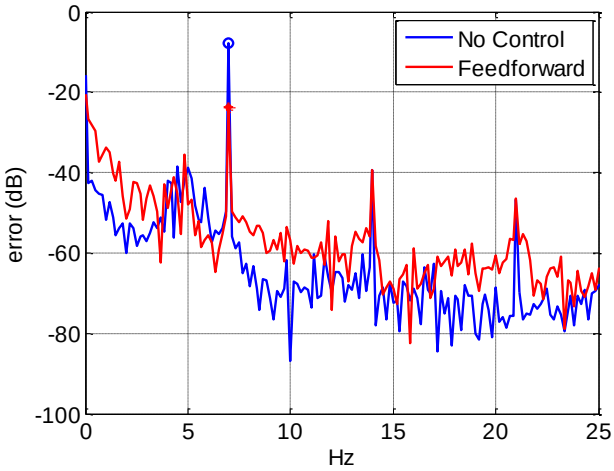

Figure 14. Spectrum of the PSD Y-axis error for elevation disturbance

Figure 15 and Figure 16 show the RMS of error for the azimuth and elevation gimbal, respectively. The horizontal axis indicates the disturbance frequency. It can be seen that the error was successfully reduced for both axes.

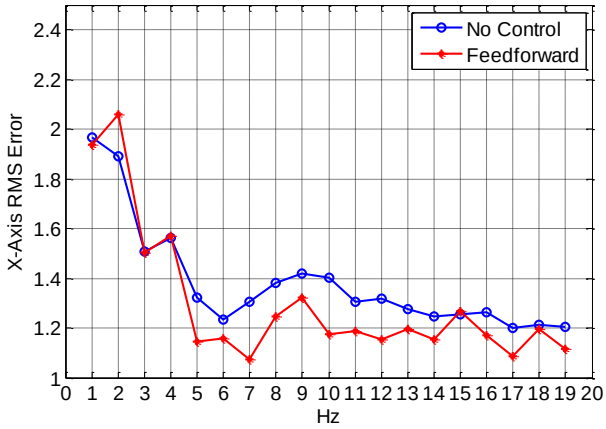

Figure 15. RMS of X-axis PSD error for azimuth disturbance

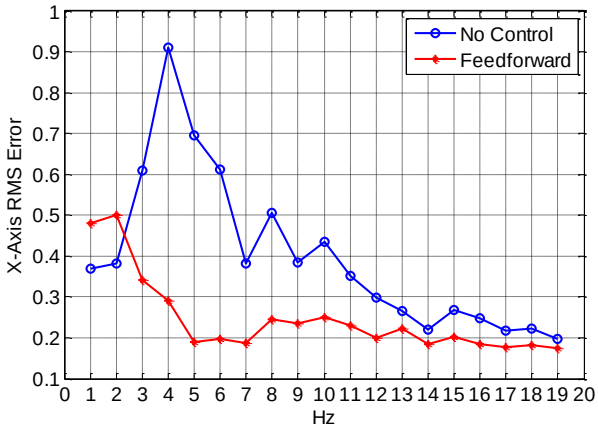

Figure 16. RMS of Y-axis PSD error for elevation disturbance

V. ADAPTIVE FILTERING FOR NFOV POINTING CONTROL

1. *Adaptive Filters*

Figure 17 shows a simple feedforward adaptive filter using an FIR filter. The function of the adaptive filter is to modify an incoming signal $x(n)$, called the reference signal, to cancel a disturbance applied to the system $d(n)$. A signal that is correlated with the disturbance is used as the reference from which the FIR filter generates a signal that cancels the disturbance by filtering the reference with weights. The error $e(n)$ measured by a sensor, which is the difference between the applied disturbance and the cancelling signal $y(n)$, is used to update the weights so that a specified cost function is minimized.

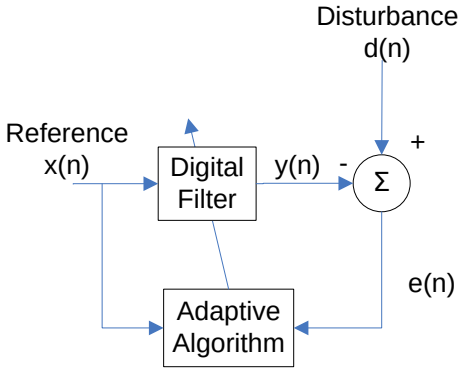

Figure 17. Simple implementation of adaptive algorithm

Adaptive filters can be infinite impulse response (IIR) or finite impulse response (FIR). IIR filters contain feedback paths in their structure and their impulse responses last indefinitely, which leads to potential instability (Haykin, 2002). FIR filters, on the other hand, contain only feedforward paths and their impulse responses die off after a finite duration, making the filter inherently stable. FIR filters are more popular than adaptive filters in real applications, and the filter used in this research is FIR. The development of the general adaptive filter algorithm presented here primarily follows those of Kuo (1996). A commonly used implementation of an FIR transverse filter structure is described in the following.

2. *Transverse Filter*

An L^{th} order transverse FIR filter has the structure shown in Figure 18. Each of the stages, or taps, delays the input signal by one sample, and this filter is sometimes called a tapped-delay line. The filter output is expressed as follows:

$$y(n) = \sum_{i=0}^{L} w_i(n)x(n-i) = \boldsymbol{w}^T(n)\boldsymbol{x}(n) \quad (19)$$

where $\boldsymbol{w}(n)$ is the filter weight vector of length whose i^{th} component is $w_i(n)$, $\boldsymbol{x}(n)$ is the vector of delayed inputs $x(n-i)$, and $y(n)$ is the filter output.

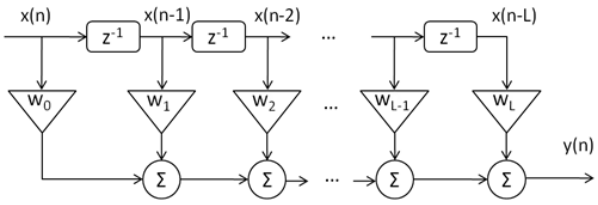

Figure 18. Transverse FIR filter structure

3. Least Mean Square and Recursive Least Square Algorithm

Lease Mean Square (LMS) and Recursive Least Square (RLS) are two common algorithms widely used to update the weights. In the LMS algorithm, the cost function $\xi(n)$ is the expectation of $e(n)^2$ called Mean Square Error (MSE), denoted by $E\{e(n)^2\}$. When the statistics of the disturbance and the reference signal are available, the weights that minimize $E\{e(n)^2\}$ can be computed. In practice, however, such a priori information is often unavailable. In the LMS algorithm, the MSE is approximated by the instantaneous squared error and the iterative steepest-gradient descent method is used to update the weights in the direction toward lowest error. The difference equation for updating weights can be expressed as:

$$\boldsymbol{w}(n+1) = \boldsymbol{w}(n) - \frac{\mu}{2}\frac{\partial J[n]}{\partial \boldsymbol{w}(n)} = \mathbf{w}(n) + \mu e(n)\boldsymbol{x}(n) \quad (20)$$

where μ is the convergence coefficient that controls the speed of the convergence to steady-state weight values.

The Recursive Least Squares (RLS) algorithm follows much of the development shown for LMS, with the important exception that it includes past data in its cost function. This accommodates nonstationary signals and usually provides faster convergence and smaller steady-state error than the LMS algorithm, though it is more computationally expensive (Kuo 1996). Instead of expressing the MSE as the instantaneous squared error signal only, the cost function becomes:

$$\xi(n) = \sum_{i=1}^{n} \lambda^{n-i} e^2(i) \quad (21)$$

where the forgetting factor, $0 < \lambda \leq 1$, allows more recent data to be weighted more heavily and data long past to be forgotten. A value of $\lambda = 1$ implies all previous error history is included in the cost function, while smaller values exclude more past errors. Typical value for λ is

$$1 - \frac{1}{2L} < \lambda < 1 \quad (22)$$

While the error and control signal expressions in RLS are identical to those of LMS, the weight update process is different. Optimal weights could be calculated from the history of all signals in the system if they are available, but keeping all previous history in digital memory is practically not possible for a long operation of the controller. Instead of calculating and inverting the correlation matrix of the reference input, $\boldsymbol{R}(n)$, the inverse correlation matrix, $\boldsymbol{Q}(n) = \boldsymbol{R}^{-1}(n)$ is calculated recursively. This eliminates the need for the inverse of $\boldsymbol{R}(n)$, greatly reducing the complexity of the RLS algorithm. The recursive equations for weight updates are:

$$\boldsymbol{z}(n) = \lambda^{-1}\boldsymbol{Q}(n-1)\boldsymbol{x}(n) \quad (23)$$

$$\boldsymbol{k}(n) = \frac{\boldsymbol{z}(n)}{\boldsymbol{z}^T(n)\boldsymbol{z}(n)+1} \quad (24)$$

$$\boldsymbol{w}(n+1) = \mathbf{w}(n) + \boldsymbol{k}(n)e(n) \quad (25)$$

where $\boldsymbol{z}(n)$ is an intermediate calculation and $\boldsymbol{k}(n)$ is the current gain vector. Finally, the inverse sample correlation matrix is updated as:

$$\boldsymbol{Q}(n) = \lambda^{-1}\boldsymbol{Q}(n-1) - \boldsymbol{k}(n)\boldsymbol{z}^T(n) \quad (26)$$

The initial condition of $\boldsymbol{Q}$ is a diagonal matrix whose component is determined by the expected variance of the measurement noise:

$$\boldsymbol{Q}(0) = \frac{1}{\sigma_m^2}\mathbf{I} \quad (27)$$

4. Filtered-X Algorithm and Bias Integration

Filtered-x is a technique to include the effect of the secondary path to avoid potential instability. As shown in Figure 19, the reference signal is passed through a model of the secondary plant, $\hat{S}(z)$ before it is fed to the adaptive algorithm. It can be applied to any weight update algorithms, and Filtered-x LMS and RLS adaptive filters are often referred as FXLMS and FXRLS, respectively. In a Filtered-x adaptive filter, the reference signal in the equations (20) and (23), are replaced by $\boldsymbol{r}(z) = \hat{S}(z)\boldsymbol{x}(z)$, whereas the input of the FIR filter is still $\boldsymbol{x}(n)$ as the output of the filter goes through the actual secondary path.

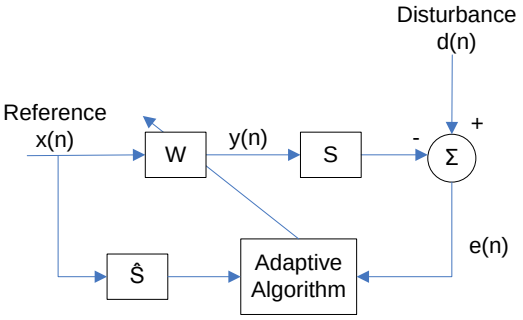

Figure 19. Filtered-x structure including secondary plant estimate prior to adaptation

In practice, it is not easy to model the secondary path precisely. But the adaptive algorithm can compensate for these uncertainties if the modeling error is not too large, and the weights updated by the algorithm should converge to the values to minimize the cost function.

The bias integration technique is originally introduced by Yoon, Bateman, et al. (2008), and modified by Corley et al. (2010). It introduces a constant reference signal for additional robustness. In bias integration, the input and weight vectors in Eq. (30) are augmented by the bias terms as follows:

$$\boldsymbol{x}[n] = \left[x(n), \quad \cdots, \quad x(n-L), \quad x_b\right]^T \quad (28)$$

$$\boldsymbol{w}(n) = \left[w_0(n), \quad \cdots, \quad w_L(n), \quad w_b(n)\right]^T \quad (29)$$

where x_b is an arbitrary constant and w_b (n) is the corresponding weight. This bias integration can be used for both FXLMS and FXRLS. The normalized Filtered-X algorithm further processes this signal $\boldsymbol{r}(n)$ by the following normalization formula, where ε is a small constant to avoid division by zero. These techniques are applied to the adaptive filters used in this research:

$$\boldsymbol{r}'(n) = \frac{\boldsymbol{r}(n)}{\boldsymbol{r}'(n)^T \boldsymbol{r}(n) + \varepsilon} \quad (30)$$

5. Adaptive Filter Experiments Using NFOV Video Tracker

The adaptive controllers were implemented on the HEL testbed for the NFOV control loop and experiments were conducted to evaluate their performance. In all experiments, the disturbance is a 5 Hz sinusoidal signal sent to the disturbance FSM. As stated earlier, this disturbance affects all three optical paths. Disturbance magnitude was 50 mV. Other natural disturbance sources include ambient mechanical vibration, power amplifiers, gyros and gimbals. It is assumed atmospheric disturbances are negligible.

The transfer functions of the proportional and integral controller in the NFOV control loop are as follows:

$$C_{AZ}(z) = -0.37164\,\frac{0.0005004\ z + 0.0005004}{z-1} \quad \text{(for AZ)} \quad (31)$$

$$C_{EL}(z) = 0.37634\,\frac{0.0005004\ z + 0.0005004}{z-1} \quad \text{(for EL)} \quad (32)$$

The adaptive filter used is a Filtered-x RLS with bias integration whose parameters are shown in Table 1. The secondary path transfer function used for Filtered-x process is:

$$P(z) = \frac{-2.6942\cdot 10^{-5}\,(z+18.45)\ (z-2.014)\ (z^2 - 2.842z + 2.267)}{(z-0.8818)\ (z^2 - 1.886z + 0.8974)\ (z^2 - 1.74z + 0.9101)} \quad (33)$$

Table 1 RLS controller parameters

Forgetting Factor	Noise Variance	Bias Integration Constant	number of weights
$\lambda = 1$	$\sigma_m^2 = 500$	$x_b = 2.0$	$L = 20$

6. Experimental Results

Figure 20 and Figure 21 show the time domain steady state error for the X asis and Y axis, respectively. Figure 22 and Figure 23 are the frequency spectrum of the errors shown in Figure 20 and Figure 21.

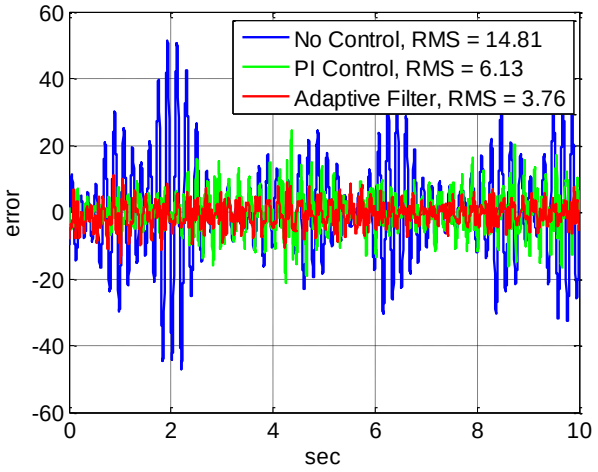

Figure 20. Time Domain Error: X-axis

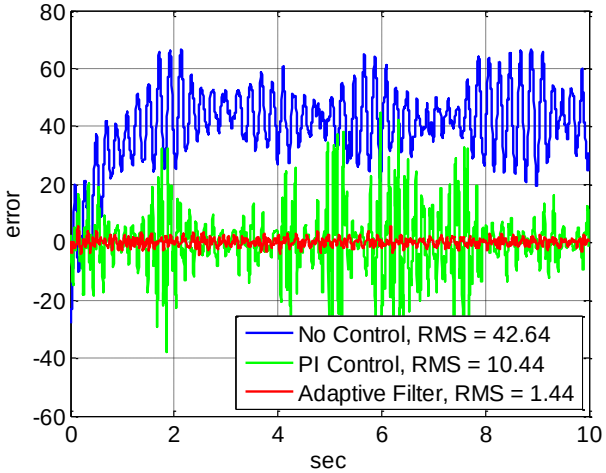

Figure 21. Time Domain Error: Y-axis

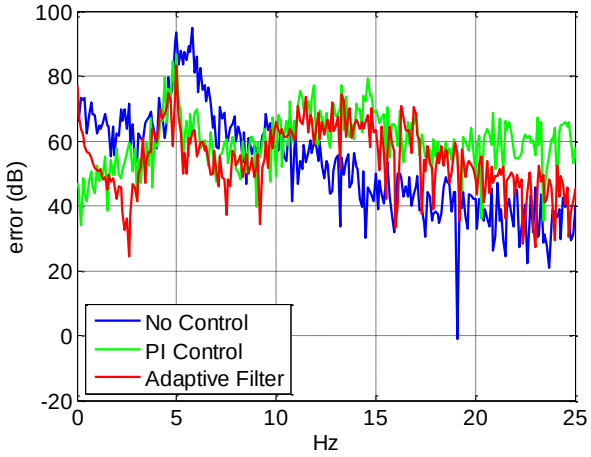

Figure 22. Frequency Domain Error: X-axis

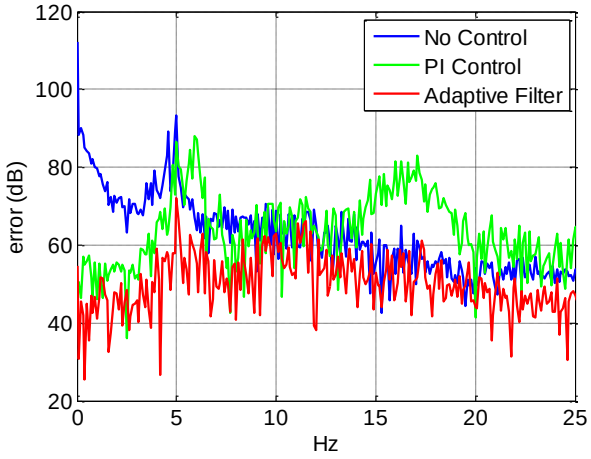

Figure 23. Frequency Domain Error: Y-axis

The frequency components other than the 5Hz, however, are not controlled disturbance and can change with time, i.e., the frequency spectrum of the disturbance may be different when the PI or the adaptive filter is applied. None the less, the overall error reduction by the adaptive filter can be seen in both axes.

VI. CONCLUSION AND FUTURE WORK

In this paper, a strap-down IRU jitter compensation method using feedforward control design is studied and tested on the testbed. It was found that designing a universal feedforward controller that will work for entire range of disturbance frequencies is problematic, and the control design relies heavily on the system setup and accurate modeling.

The current feedforward control results were based on 2 Hz to 15 Hz sinusoidal disturbances through the telescope gimbals. More tests are currently being performed using various disturbance profiles with method 2 shown in Figure 4(b). It is likely that the difference in the strap-down IRU setup in method 2 can mitigate certain problems associated with flexible telescope structures observed in the current results.

An adaptive filtering method for narrow-field-of-view video tracker jitter correction is also presented. Seamless integration of jitter control and fine steering is an important task. The poor performance of the strap-down IRU system compared to the platform-based IRU system is due to the lack of good inertial feedback information. The video tracker or additional on-board sensors may be useful to update feedforward control design and improve the overall performance of the strap-down IRU system.

REFERENCES

[1] Perram, G, Cusumano, S., Hengehold R., and Fiorino, S., "Introduction to Laser Weapon Systems", Directed Energy Professional Society, 2010.

[2] Widrow, B., & Stearns, S. D. "Adaptive signal processing", Upper Saddle River: Prentice-Hall, Inc, 2002.

[3] Elliott, S. J., & Nelson, P. A., "The application of adaptive filtering to the active control of sound and vibration", ISVR: Technical Report 136, 1985.

[4] Haykin, S., "Adaptive filter theory", Upper Saddle River: Prentice-Hall, Inc, 2002.

[5] Kuo, S. M., & Morgan, D. R., "Active noise control systems", New York: John Wiley & Sons, Inc., 1996.

[6] Edwards, S. G., "Active narrowband disturbance rejection on an ultra quiet platform", Monterey: NPS PhD Dissertation, 1999.

[7] Watkins, J. R., & Agrawal, B. N, "Use of least mean squares filter in control of optical beam jitter", AIAA Journal of Guidance, Control, and Dynamics, 30(4), 2007.

[8] Yoon, H., et al., "Laser beam jitter control using recursive-least-squares adaptive filters", DEPS Beam Control Conference, 2008.

[9] Yoon, H., Bateman, B.E. & Agrawal, B.N., "Laser Beam Jitter Control Using Recursive-Least-Square Adaptive Filters", Directed Energy Systems Symposium Beam Control Conference Proceedings. Monterey, California, CA, 2008.

[10] Corley, C.M.S., Nagashima, M. & Agrawal, B.N., "Beam control and a new laboratory testbed for adaptive optics in a maritime environment", IEEE Aerospace Conference. Big Sky, Montana, USA, 2010.